Ginsenoside Rg3 potentiates cisplatin antitumor activity while mitigating nephrotoxicity through SIRT1-mediated suppression of the NLRP3 inflammasome

JINGHUI ZHAI[1], YUEMING ZHANG[1], JIAWEI GONG[1], LI FU[2] and SIXI ZHANG[1,3]

[1]Department of Clinical Pharmacy, The First Hospital of Jilin University, Changchun, Jilin 130021, P.R. China; [2]Department of Research, Dalian Fusheng Natural Medicine Development Co., Ltd., Dalian, Liaoning 116600, P.R. China; [3]School of Pharmaceutical Science, Jilin University, Changchun, Jilin 130000, P.R. China

Received September 11, 2025; Accepted April 15, 2026

DOI: 10.3892/ijmm.2026.5870

Abstract. Lung cancer is one of the most common causes of cancer-related mortality worldwide, with cisplatin (CP) being a key chemotherapeutic agent. However, its use is limited by nephrotoxicity and drug resistance. Ginsenoside Rg3 (Rg3) has anticancer properties and potential protective effects on normal tissues. The present study investigated the therapeutic effect of Rg3 and CP in suppressing the proliferation of lung carcinoma cells (LLCs) and inhibiting tumor growth, using both *in vitro* and *in vivo* models. LLC cells were exposed to Rg3 and/or CP and the effects on cell proliferation were measured by MTT assay. Tumor-bearing mouse models were constructed to evaluate the impact on tumor growth. Modulation of biological pathways was analyzed using flow cytometry, western blotting and immunohistochemistry. Co-treatment with Rg3 and CP enhanced apoptosis in LLC cells and tumor tissues by upregulating cleaved caspase-3/9 and phosphorylated (p-) p53, while suppressing vascular cell adhesion molecule 1, intercellular adhesion molecule 1 (ICAM1), macrophage migration inhibitory factor (MIF) and p-p65 activation. The downregulation of Organic Cation Transporter 2 (OCT2) and P-glycoprotein (P-gp) expression in renal tissues of xenograft mice by Rg3 may explain its dual effects in alleviating CP nephrotoxicity and reversing drug resistance. Mechanistic studies in HK-2 cells demonstrated that Rg3 (80 μg/ml) attenuated CP-induced NLRP3 inflammasome activation (NLRP3, apoptosis-associated speck-like protein with CARD (ASC), caspase-1) and p-p65 expression; these effects were reversed by the SIRT1 inhibitor Ex527, implicating SIRT1 pathway dependency. Molecular docking provided a hypothetical model for binding of Rg3 to SIRT1 (-7.492 kcal/mol) and NLRP3 (-6.764 kcal/mol), providing a structural basis for the regulatory interactions. Rg3 showed potential as a renal protector, anti-inflammatory agent and adjunct to CP chemotherapy. The combination offers a promising therapeutic strategy for lung cancer by enhancing efficacy and decreasing nephrotoxicity. Further investigation into mechanisms and long-term effects is warranted.

Correspondence to: Professor Sixi Zhang, Department of Clinical Pharmacy, The First Hospital of Jilin University, 1 Xinmin Street, Changchun, Jilin 130021, P.R. China
E-mail: sixi@jlu.edu.cn

Dr Li Fu, Department of Research, Dalian Fusheng Natural Medicine Development Co., Ltd., 5 Tianshan Street, Dalian, Liaoning 116600, P.R. China
E-mail: dlfulii@aliyun.com

Key words: ginsenoside Rg3, cisplatin, antitumor, SIRT1/NLRP3 pathway, renal injury

Introduction

Lung cancer (LC) is the most common cause of cancer-associated mortality and worldwide, and the predominant subtype is non-small cell LC (NSCLC) (1,2). Chemotherapy, particularly with drugs such as cisplatin (CP), has long been a cornerstone in cancer treatment. However, its efficacy is frequently restricted by dose-dependent toxicity, including nephrotoxicity, and the development of drug resistance (3-5). Identifying novel therapeutic approaches that can boost the effectiveness of chemotherapeutic agents and mitigate their adverse effects is a priority in cancer treatment research (5,6).

Previous studies have highlighted the potential of natural compounds in modulating cancer treatment outcomes (7-9). Ginsenoside Rg3 (Rg3), which is isolated from ginseng, exhibits pharmacological activity, including anti-tumor, antidiabetic, immunomodulation, anti-inflammation and cardiovascular protection effects (10-12). Rg3 inhibits the angiogenesis of pulmonary and lung carcinoma (13,14). The use of Rg3 in combination with chemotherapeutic drugs has been shown to improve treatment outcomes and diminish chemotherapy toxicity (12). Jiang *et al* (15) demonstrated that Rg3 can reduce the expression of NF-κB, programmed death ligand-1 and Akt (13). Rg3 may enhance sensitivity to CP by blocking NF-κB pathway activation (14). However, the role of Rg3 in amplifying the therapeutic effects of CP in lung tumor-bearing mice remains unclear.

Our previous investigation (20) demonstrated that Rg3 protects against CP-induced nephrotoxicity via

autophagy-mediated NOD-like receptor pyrin domain-containing protein 3 (NLRP3) inflammasome suppression, however the renoprotective effects were investigated only in healthy mice, without validation in tumor-bearing animals. Consequently, it is uncertain whether Rg3 exerts similar renal protection in a cancer setting without compromising CP antitumor efficacy. Moreover, the renal accumulation of Rg3 and CP, which governs both therapeutic efficacy and nephrotoxic burden, is modulated by kidney-specific transporters such as organic cation transporter 2 (OCT2) and P-glycoprotein (P-gp). To elucidate this mechanism and provide a more comprehensive understanding of Rg3-mediated renal protection, the present study investigated how OCT2 and P-gp regulate the renal uptake and efflux of Rg3 and CP, thereby affecting their intrarenal accumulation and nephrotoxic potential. To the best of our knowledge, the present study is the first to evaluate Rg3 + CP efficacy and nephroprotection simultaneously in an *in vivo* Lewis lung carcinoma cells (LLC) allograft model.

The sirtuin (Sirt)1/NLRP3 pathway is involved in the inflammatory response (17) and serves a protective role against drug-induced organ injury. Quercetin and calycosin ameliorate isonicotinic acid hydrazide (INH)-induced liver toxicity and doxorubicin-induced cardiotoxicity, respectively, by modulating this signaling axis (18,19). These findings collectively underscore the therapeutic potential of targeting SIRT1/NLRP3 signaling as a common mechanism to mitigate chemically induced tissue damage across different organ systems. Therefore, it was hypothesized that the SIRT1/NLRP3 pathway may mediate the renoprotective effects of Rg3 against CP-induced nephrotoxicity.

Materials and methods

Materials. .0% purity, batch no. 20170206; Fig. 1A; Dalian Fusheng Natural Medicine Development Co., Ltd.) was dissolved in DMSO to a concentration of 10 g/ml as a stock solution, which was stored at -20˚C for subsequent use. CP (batch no. 170905) was obtained from Jiangsu Haosen Co. at a concentration of 100 mM. SIRT1 (13161-1-AP, 1:1,000), NLRP3 (27458-1-AP, 1:1,000), p65 (80979-10RR, 1:1,000) and phosphorylated (p-)p65 (82335-1-RR, 1:1,000) were from Proteintech. Macrophage migration inhibitory factor (MIF) (ab7207, 1:2,000), p53 (ab32049, 1:2,000), p-p53 (ab33889, 1:1000), P-gp (ab170904, 1:1,000), OCT2 (ab179808, 1:5,000), vascular cell adhesion molecule 1(VCAM1, ab134047, 1:2,000) and intercellular adhesion molecule 1(ICAM1, ab282575, 1:1,000) were from Abcam. Caspase-3 (YM8058, 1:1,000) was from Immunoway, and Caspase-9 (cat. no. AF1264, 1:1,000) was from Beyotime (Table SI). EX527 was from Selleck. Anti-rabbit IgG (A0208, 1:1,000), Anti-mouse IgG (A0216, 1:1,000) and GAPDH (AF0006, 1:1,000) were obtained from Beyotime Biotechnology. The Alexa Fluor 488-goat anti-rabbit secondary antibody (abs20025, 1:100) was acquired from Absin Biotechnology Company.

Cell culture. LLC and human renal tubular (HK-2) cells were obtained from the School of Pharmacy, Jilin University (Changchun, China). RPMI-1640 medium, DMEM/F12, penicillin, streptomycin and fetal bovine serum were purchased from Absin (Shanghai) Biotechnology Co., Ltd. LLC cells were cultivated in RPMI-1640 medium containing 10% fetal bovine serum, 100 μg/ml streptomycin and 100 U/l penicillin. Cells were kept at 37˚C in a 5% CO_2 humidified atmosphere. HK-2 cells were cultured in DMEM/F12 under the same conditions. Cell cultures were passaged every 2-3 days and passages 3-8 were utilized for subsequent experiments.

LLC cells were treated with CP (100, 200, 400, 800 and 1,600 nM), Rg3 (10, 20, 40 and 80 μg/ml) or CP (100 nM) + Rg3 (20, 40 and 80 μg/ml) for 4, 12, 24 and 48 h at 37˚C. HK-2 cells were treated with CP (10 μM), Rg3 (80 μg/ml), Ex527 (30 μM), CP (10 μM) + Rg3 (80 μg/ml) or CP (10 μM) Ex527 (30 μM) at 37˚C.

Cell viability assay. Cell viability was assessed using the MTT assay (Sigma-Aldrich; Merck KGaA). Briefly, cells were seeded in 96-well plates at $1x10^4$ cells/well. A total of 10 μl 5 mg/ml MTT solution was added to each well for 4 h. The supernatant was discarded, and 150 μl DMSO was added to each well to dissolve the formazan crystals. Absorbance was measured at 490 nm using a Microplate Reader (Agilent Technologies). Each experiment condition was replicated six times, and cell viability was calculated relative to the untreated control group.

Wound healing assay. The LLC cells were seeded (without serum) in 6-well plates at $5x10^4$ cells/well and cultured to 100% confluence. Sterile pipette tips were used to create 100 μm wounds. Cells were treated with CP (100 nM) in the presence or absence of Rg3 (20, 40 and 80 μg/ml) for 24 h at 37˚C. Olympus CKX41 light microscope was used to capture images.

Immunofluorescence analysis. HK-2 cells were seeded in 6-well plates ($1x10^5$/well). Following overnight incubation at 37˚C, they were treated at 37˚C for 24 h with CP (10 μM), CP (10 μM) + Rg3 (80 μg/ml), CP (10 μM) + Rg3 (80 μg/ml) + Ex527 (30 μM) or Ex527 (30 μM). Cells were washed four times with cold PBS, fixed at room temperature with 4% paraformaldehyde for 10 min and permeabilized with 0.5% Triton X-100 for 15 min at room temperature. Following three 5 min PBS washes, cells were blocked with 5% BSA (Sigma-Aldrich; Merck KGaA) at 37˚C for 1 h, then incubated overnight at 4˚C with rabbit anti-NLRP3 antibody (cat. no. 27458-1-AP, 1:100). Following three PBS washes, cells were incubated with the Alexa Fluor 488-goat anti-rabbit secondary antibody (cat. no. abs20025, 1:100, Absin) at room temperature for 1 h in the dark. Following three PBS washes, cells were stained with DAPI at room temperature for 5-10 min. Fluorescence images were captured using a BX83 fluorescence microscope (Olympus Corporation). Images were analyzed using ImageJ software (version 1.52a, National Institutes of Health).

Detection of superoxide dismutase (SOD), malondialdehyde (MDA), catalase (CAT) and lactate dehydrogenase (LDH). SOD (A001-302), MDA (A003-401), CAT (A007-1-1) and LDH (A020-2-2) Assay kits (Nanjing Jiancheng Bioengineering Institute) were used to assess intracellular SOD, MDA, CAT and LDH levels according to the manufacturer's instructions.

Molecular docking. The structure of Rg3 was retrieved from the PubChem database (https://pubchem.ncbi.nlm.nih.gov/),

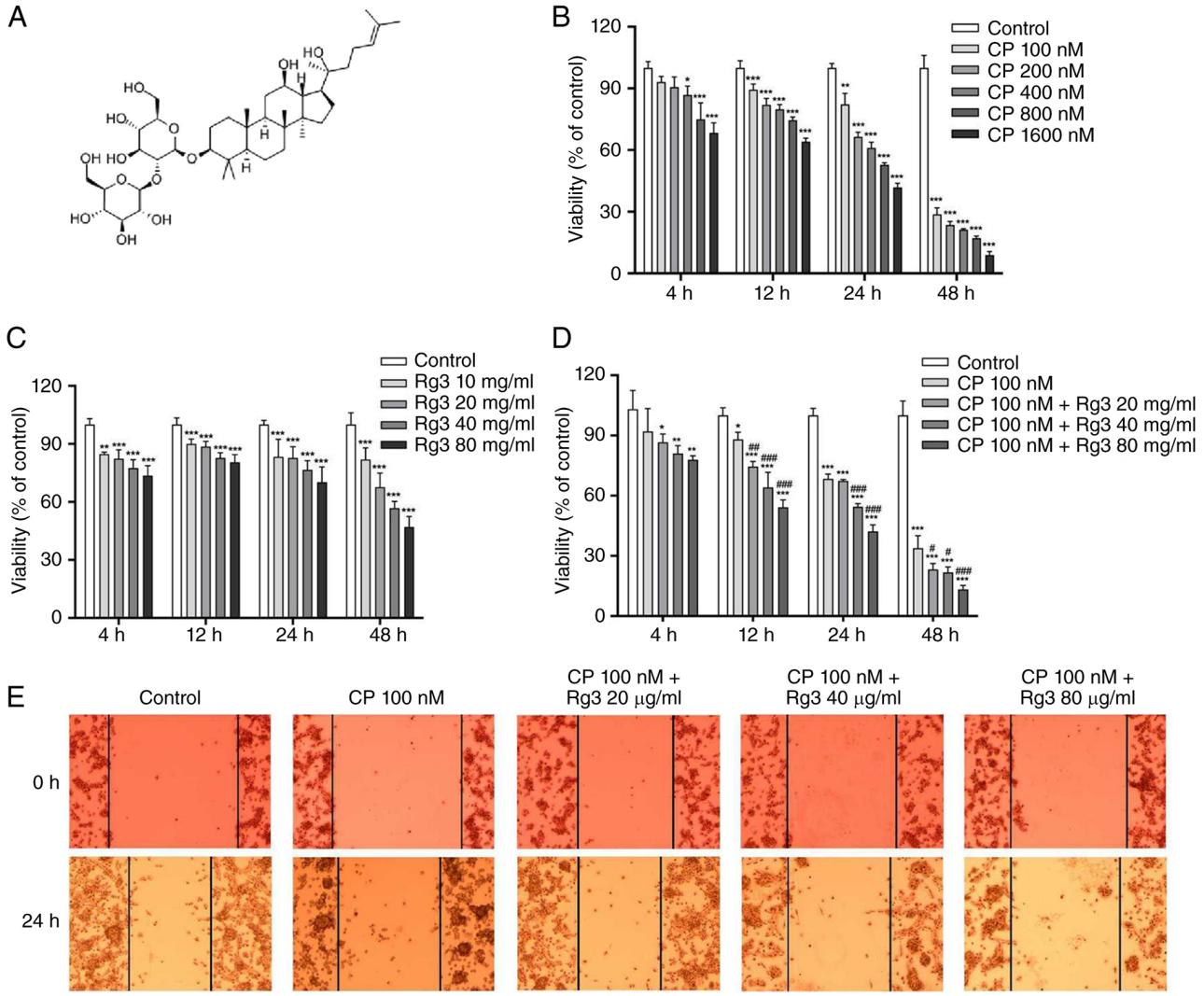

Figure 1. Effect of Rg3 and CP on LLC cell viability and migration. (A) Chemical structure of Rg3. (B) Effect of CP and (C) Rg3 on cell viability. Effect of CP + Rg3 on cell (D) viability and (E) migration. Magnification, x20. *P<0.05, **P<0.01, ***P<0.001 vs. control; $^{\#}$P<0.05, $^{\#\#}$P<0.01, $^{\#\#\#}$P<0.001 vs. CP. Rg3, ginsenoside Rg3; LLC, Lewis lung carcinoma; CP, cisplatin.

and imported into Chem3D software (Chem3D Pro 21.0, revvitysignals.flexnetoperations.com/), where it underwent optimization and energy minimization using the MM2 module. The structures of NLRP3 (ID: 7ALV) and SIRT1 (ID: 4ZZI) were acquired from Research Collaboratory for Structural Bioinformatics Protein Data Bank (rcsb.org/). These structures were processed within the Maestro11.9 (Schrödinger, Inc.) platform employing Schrodinger's Protein Preparation Wizard. This processing involved removal of crystalline water molecules, addition of missing hydrogen atoms, repair of missing bond information and patching of incomplete peptide segments. Finally, the proteins were energy-minimized and geometrically optimized. The binding affinity between NLRP3, SIRT1 and Rg3 was evaluated based on binding energy and the virtual docking model was visualized using Pymol2.1 software (Schrödinger, LLC).

Xenograft tumor mouse model. All animal care and experimental procedures were approved by the Center for Experimental Animal Research of the Institute of Basic Medical Sciences, Jilin University (Changchun, China; approval no. 2023226). The experiments with animal followed an Animal Research: Reporting of *In Vivo* Experiments protocol (15). All animal procedures were performed in strict accordance with the guidelines (16) for tumor-bearing mice established by the Center for Experimental Animal Research, Institute of Basic Medical Sciences, Jilin University. Male Kunming mice (n=32; age, 4-6 weeks; weight, 22±2 g) were purchased from the Center of Experimental Animals of Baiqiuen Medical College of Jilin University (Jilin, China). Mice were allowed free access to food and water and were maintained on a 12/12-h light/dark cycle at a temperature of 20-25˚C and humidity of 50±5%. Tumors were induced by subcutaneous injection of $4x10^6$ LLC cells in 200 μl PBS into the right axilla. Tumor-bearing mice were randomized using a computer-generated random number sequence (Excel 2019, Microsoft Corporation) with block randomization and allocation concealment using sequentially numbered, sealed envelopes prepared by an independent technician; investigators conducting tumor measurements and tissue analysis were blinded to group allocation throughout the experiment. Mice were grouped (n=8/group) as follows: i) Control, receiving

intraperitoneal (IP) injection of 0.9% NaCl and daily oral water gavage; ii) CP, receiving IP injection of CP at 4 mg/kg every 2 days, and daily oral water gavage; iii) CP + Rg3, receiving IP injection of CP at 4 mg/kg every 2 days, and daily oral Rg3 (5 mg/kg); and iv) Rg3, receiving daily oral Rg3 (5 mg/kg), as previously described (20) (Fig. S1). Administration was initiated when tumor volumes reached 50 mm^3. The tumor volume and body weight were measured every 2 days post-inoculation, with tumor volume calculated as 1/2x tumor length x tumor $width^2$. Humane endpoints were tumor diameter ≥15 mm and >20% body weight loss. Following the 10 day drug administration period, no animals were excluded from the final analysis. The blood was collected via abdominal aortic puncture. Mice were euthanized using CO_2 inhalation (chamber volume displaced by the CO_2 flow rate, 30%). Death was confirmed by absence of response to external stimuli, such as a gentle prod with a blunt object and the cessation of heartbeat and breathing. Tumors and kidneys were immediately excised in an aseptic manner for analysis.

Assessment of tumor/body weight index. Prior to euthanasia, mouse body weight was measured. Tumors were surgically removed following euthanasia, dried with filter paper and weighed. Tumor-to-body weight ratio was calculated as (tumor weight/body weight) x100%.

Histopathological and immunohistochemical analyses. Tumor tissue was fixed in 10% formalin at room temperature for 24 h, embedded in paraffin and sectioned at 4 μM. These sections underwent deparaffinization, rehydration and hematoxylin-eosin staining at room temperature (hematoxylin for 5 min and eosin for 2 min), with histopathological changes examined at 400X magnification via a light microscope (Nikon Corporation; Eclipse TS200). Kidney tissue was fixed in 10% neutral buffered formalin at room temperature for 24 h, then embedded in paraffin and sectioned at 4 μM. Sections were mounted on glass slides and dried overnight at 37˚C. Paraffin sections were deparaffinized in xylene twice for 10 min each, then rehydrated through a graded ethanol series, followed by rinsing in PBS. Antigen retrieval was performed by heating in 10 mM sodium citrate buffer (pH 6.0) in a microwave oven at 95-100˚C for 15-20 min. After cooling to room temperature, sections were washed three times with PBS for 5 min each. Deparaffinized sections were treated with 3% hydrogen peroxide (v/v) in methanol for 15 min at room temperature, followed by washing twice with PBS. Non-specific binding was blocked with 10% BSA at room temperature for 30 min. Sections were incubated with primary antibody against OCT2 (1:100, ab179808, Abcam) overnight at 4˚C in a humidified chamber. After washing three times with PBS for 5 min each, sections were incubated with the Alexa Fluor 488-goat anti-rabbit secondary antibody (cat. no. abs20025, 1:100 dilution, Absin) at room temperature for 30 min. Immunoreaction products were observed under a light microscope (Olympus BX53). Images were captured and analyzed using ImageJ software (version 1.52a, National Institutes of Health).

TUNEL assay. Apoptosis was identified using the TUNEL kit. Kidney tissue was fixed in 10% neutral buffered formalin at room temperature for 24 h, embedded in paraffin and sectioned at 4 μM. Sections were mounted on glass slides and dried overnight at 37˚C. Paraffin sections were deparaffinized in xylene twice for 10 min each, then rehydrated through a graded ethanol series (100, 95, 85, 75, and 50% ethanol, 2 min each), followed by rinsing in phosphate-buffered saline (PBS). Sections were permeabilized with Proteinase K (20 μg/ml) in PBS at 37˚C for 30 min, followed by washing twice with PBS. TUNEL staining was performed using the TUNEL BrightGreen Apoptosis Detection kit (Beyotime Biotechnology, cat. no. C1088) according to the manufacturer's instructions. Briefly, sections were incubated with TUNEL reaction mixture at 37˚C for 60 min in a humidified chamber protected from light. Sections were stained with DAPI (1 μg/ml) at room temperature for 5-10 min, then rinsed three times with PBS. Sections were mounted with antifade mounting medium (Vector Laboratories, H-1700 or Fluoromount-G) and covered with glass coverslips. TUNEL-positive cells were visualized using a fluorescence microscope (Nikon Eclipse TS200). For each tissue section, three randomly selected fields of view were captured. TUNEL-positive (green fluorescent) cells and total cells (DAPI-stained blue nuclei) were counted, and the apoptotic index (%) was calculated as follows: (number of TUNEL-positive cells/total number of DAPI-stained nuclei) x100%.

Western blot analysis. Cells were rinsed with cold PBS and lysed in RIPA buffer (Beyotime Biotechnology) supplemented with 1% (w/v) PMSF. Tumor and kidney tissue were minced and homogenized in RIPA buffer containing 1% PMSF on ice. Cell suspensions and tissue homogenates were centrifuged at 15,000 g for 15 min at 4˚C. Protein concentrations were determined using the bicinchoninic acid method. Aliquots containing 30 μg protein per lane were mixed with 5X loading buffer and heated at 100˚C for 5 min to denature. Protein samples were separated by 10-12% SDS-PAGE and transferred to PVDF membranes. Membranes were blocked with 5% non-fat milk in TBST (0.1% Tween-20) at room temperature for 1 h, followed by overnight incubated with primary antibodies at 4˚C. The primary antibodies were as follows: SIRT1 (1:1,000 dilution, 13161-1-AP, Proteintech) , NLRP3 (1:1,000, 27458-1-AP, Proteintech) , p65 (1:1,000 dilution, 80979-10RR, Proteintech) , p-p65 (1:1,000 dilution, 82335-1-RR, Proteintech), MIF (1:1,000 dilution, ab7207, Abcam), p53 (1:2,000 dilution, ab32049, Abcam), p-p53 (1:2,000 dilution, ab338899, Abcam), P-gp (1:1,000 dilution, ab170904, Abcam), OCT2 (1:5,000 dilution, ab179808, Abcam), VCAM1 (1:2,000 dilution, ab134047, Abcam), ICAM1 (1:1,000 dilution, ab282575, Abcam), Caspase-3 (1:1,000 dilution, YM8058, Immunoway), Caspase-9 (1:1,000 dilution, AF1264, Beyotime), and GAPDH (1:1,000 dilution, AF0006, Beyotime) at 4˚C. After washing with TBST, membranes were incubated with HRP-conjugated secondary antibodies (cat. nos. A0208, 1:1,000, Anti-mouse IgG, A0216, 1:1,000, Beyotime) at room temperature for 1 h. Protein bands were detected using an ECL kit (New Cell & Molecular Biotech Co., Ltd.), and visualized on X-ray film (Kodak). Band images were quantified using ImageJ 1.37c software (National Institutes of Health).

Statistical analysis. GraphPad Prism 9.0 software (Dotmatics) was employed for statistical analysis. Data are presented as the mean ± standard error of the mean from ≥3 independent

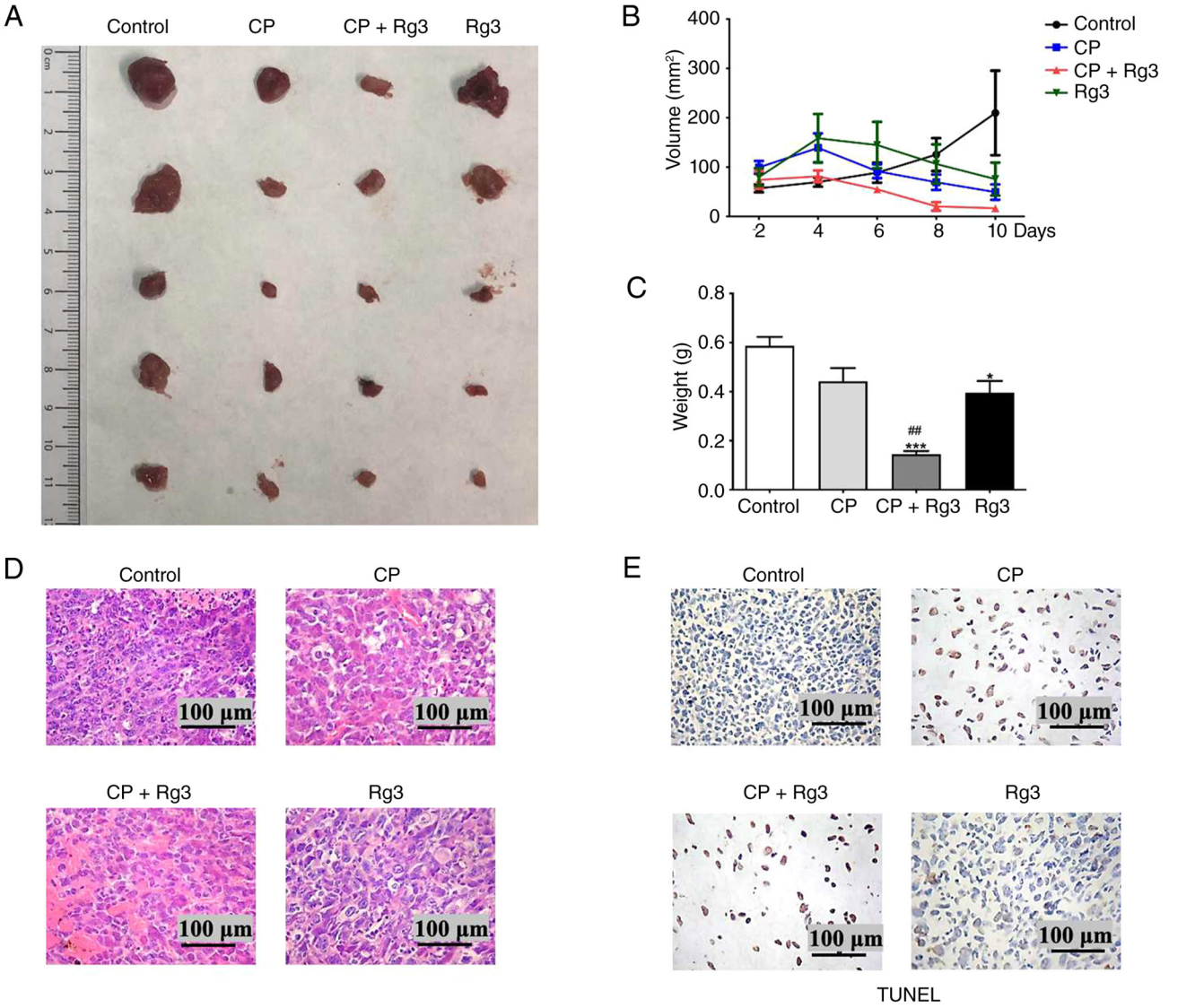

Figure 2. Effect of CP and Rg3 on xenograft tumor mice. Effects of CP and Rg3 on (A) tumor (B) volume and (C) weight. (D) Effect of CP and Rg3 on histopathology of mouse tumor. Magnification, x200. (E) Effect of CP and Rg3 on apoptosis of cells. *P<0.05, ***P<0.001 vs. control. $^{\#\#}$P<0.01 vs. CP. CP, cisplatin; Rg3, ginsenoside Rg3.

experiments. One-way ANOVA followed by Tukey's post hoc test was applied. P<0.05 was considered to indicate a statistically significant difference.

Results

CP and Rg3 decrease LLC cell viability in a dose- and time-dependent manner. MTT assay was employed to measure cell viability (17). The findings revealed that both CP and Rg3 reduced LLC cells viability in dose- and time-dependent manner (Fig. 1B-D). The combination of Rg3 and CP resulted in a time-dependent decrease in cell viability, with significant reductions at 12, 24 and 48 h compared with CP treatment alone. CP + Rg3 (40 and 80 μg/ml) groups exhibited slower migration than the CP group (Figs. 1E and S2). These results indicated that Rg3 enhanced therapeutic efficacy of CP.

Rg3 and CP co-treatment enhances anti-tumor effects in an LLC Xenograft Mouse Model. To evaluate whether Rg3 enhances CP anti-tumor activity *in vivo*, tumor volume and weight were measured in a xenograft model. There was no significant difference in tumor volume between any groups. Only the CP + Rg3 group exhibited significantly decreased tumor weight compared with CP group (Fig. 2A-C). This suggests that Rg3 increased CP antitumor effect and slowed tumor growth.

HE and TUNEL staining were used for histopathological analysis. Tumor cells were closely packed with clear nucleoli and a diffuse pattern. The CP + Rg3 group demonstrated a larger area of unclear borders with cell nucleus disappearance compared with CP alone, supporting a role of Rg3 in enhancement of chemosensitivity (Fig. 2D). The TUNEL assay demonstrated increased apoptosis in the co-treatment group, as indicated by higher brown staining intensity (Fig. 2E). This suggested that the combination of CP and Rg3 enhanced tumor cell apoptosis.

Rg3 combined with CP promotes p53, caspase-3 and caspase-9 expression. Western blotting was performed to quantify the

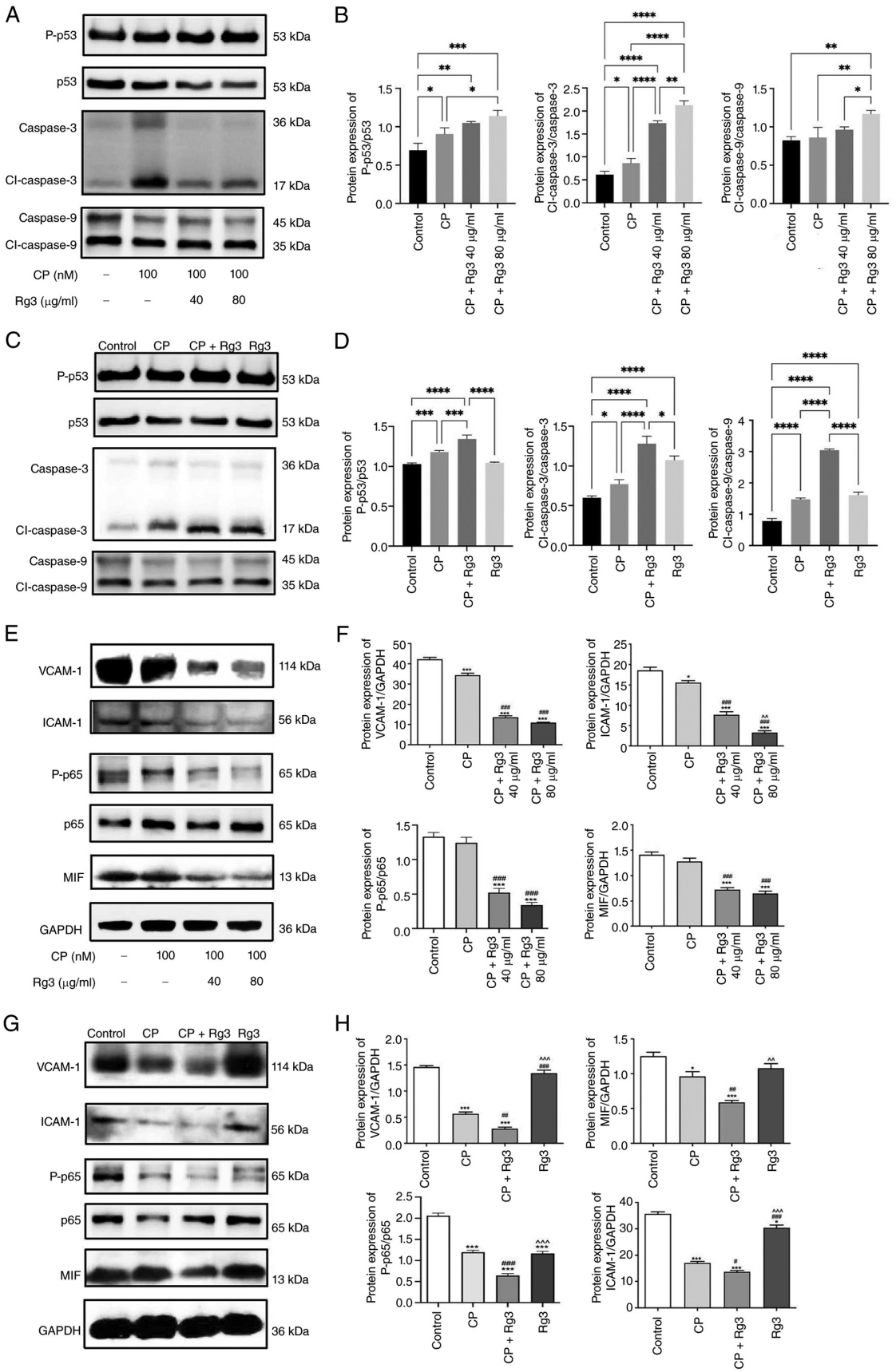

Figure 3. Effect of CP and Rg3 on the expression of p53, caspase-3, caspase-9, VCAM-1, ICAM-1, p-p65 and MIF in LLC cells and tumor tissue. (A) Western blots and (B) quantification of p-p53/p53, Cl-caspase-3/caspase-3, Cl-caspase-9/caspase-9. (C) Western blots and (D) quantification of p-p53/p53, Cl-caspase-3/caspase-3, Cl-caspase-9/caspase-9 in tumor tissue. (E) Western blots and (F) quantification of protein bands showing expression levels of VCAM-1, ICAM-1, p-p65/p65, MIF and GAPDH in cells. (G) Western blots and (H) quantification of protein bands showing expression levels of VCAM-1, ICAM-1, p-p65/p65, MIF and GAPDH in tumor tissue. *P<0.05, **P<0.01, ***P<0.001, ****P<0.0001 vs. control. $^{\#}$P<0.05, $^{\#\#}$P<0.01, $^{\#\#\#}$P<0.001 vs. CP group. ^^P<0.01, ^^^P<0.001 vs. CP + Rg3 (40 μg/ml) group. CP, cisplatin; Rg3, ginsenoside Rg3; VCAM, vascular cell adhesion molecule; ICAM, intercellular adhesion molecule; p-, phosphorylated; MIF, macrophage migration inhibitory factor; cl, cleaved.

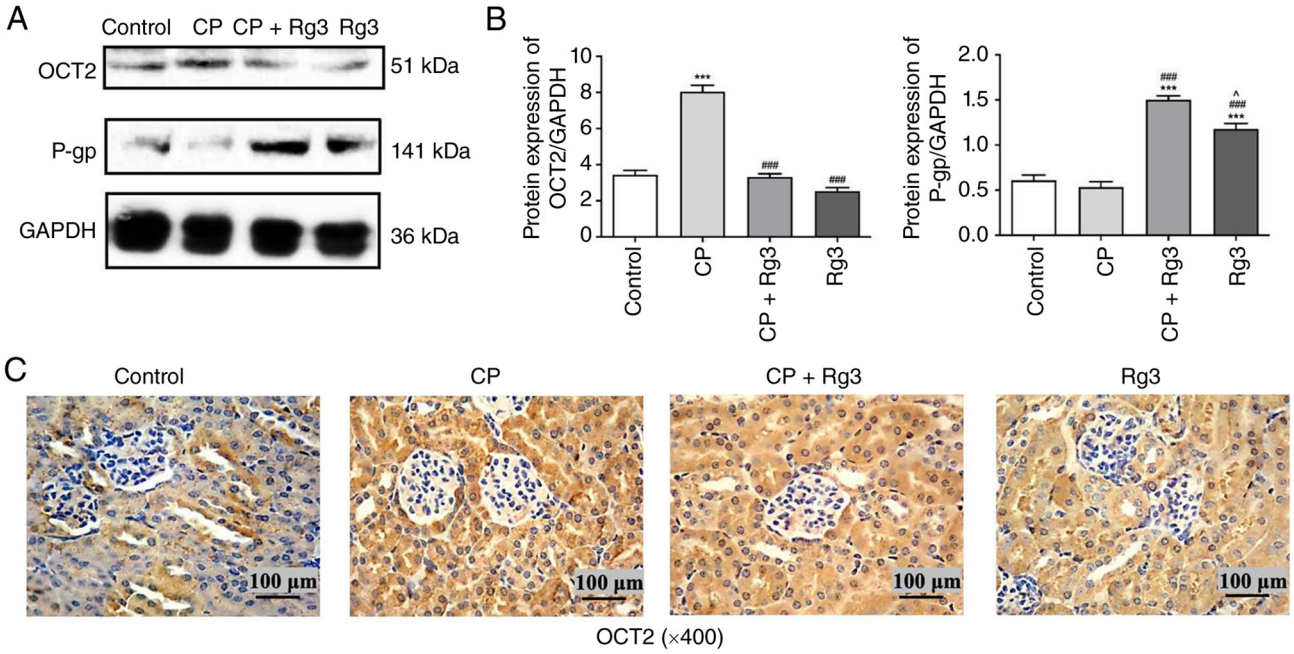

Figure 4. Effect of CP and Rg3 on the expression of OCT2 and P-gp in kidney tissue. (A) Representative western blot images and (B) Quantitative analysis of western blot data. (C) Immunohistochemical analyses of OCT2 in kidney tissue. ***P<0.001 vs. control. ###P<0.001 vs. CP. ^P<0.05 vs. CP + Rg3. CP, cisplatin; Rg3, ginsenoside Rg3; OCT2, Organic Cation Transporter 2; P-gp, P-glycoprotein.

alterations in apoptotic protein expression following treatment with CP and Rg3. Rg3 significantly elevated the levels of cleaved caspase-3 and -9 and p-p53, which are pivotal for apoptosis (18,19), both in LLC cells and tumor tissue (Fig. 3A-D). The enhancement in these apoptotic markers following CP + Rg3 treatment suggested a potential therapeutic strategy to induce programmed cell death.

Combined Rg3 + CP treatment inhibits VCAM-1, ICAM-1, MIF and NF-κB-mediated inflammation. Western blot analysis was performed to assess the effects of Rg3 and CP on the expression of VCAM-1, ICAM-1, p-p65 and MIF in LLC cells and mouse tumor tissue samples (Fig. 3E-H). Notably, the co-treatment with Rg3 + CP resulted in a significant downregulation of VCAM-1 and ICAM-1 compared with CP alone. This reduction in adhesion molecules suggested that Rg3 may influence cell interactions and migration, which are key in tumor progression (20). Furthermore, the expression of p-p65, a marker of NF-κB pathway activation, was decreased in the presence of Rg3, indicating its potential to inflammatory responses. Similarly, MIF, a key molecule in immune cell function (21), showed decreased expression, indicating that Rg3 altered the tumor immune microenvironment. These results collectively suggested that Rg3, when administered with CP, modulated proteins involved in cell adhesion, inflammation and immune regulation, underscoring its potential as a therapeutic agent in cancer and immune modulation.

Effects of Rg3 on expression of OCT2 and P-gp in mouse kidneys. The expression of OCT2, a key organic cation transporter (21), was elevated by CP. However, this increase was counteracted when Rg3 was added with CP (Figs. 4A-C and S3). Similarly, the expression of P-gp, a membrane-bound drug efflux pump (22), was significantly enhanced by Rg3. P-gp expression in the Rg3 group was 1.5-2.0-fold higher than that in the control group, indicating a significant upregulation of P-gp in response to Rg3 (Fig. 4A and B). These results demonstrated that Rg3 had a significant impact on the expression of both OCT2 and P-gp in renal tissue. Consequently, Rg3 may decrease the accumulation of CP in the kidney, potentially mitigating its nephrotoxic effects.

High-affinity binding of Rg3 with SIRT1 and NLRP3. Rg3 exhibited strong binding affinity with both the SIRT1 and NLRP3 target proteins, as evidenced by their high docking scores (Fig. 5A and B), with binding energies of -7.492 and -6.764 kcal/mol, respectively. Visualization of the docked compound-protein complexes demonstrated the binding modes of the compounds within the protein pockets, including interactions with specific amino acid residues. Rg3 demonstrated binding with the active sites of both SIRT1 and NLRP3 target proteins, as well as favorable docking scores, indicating the formation of stable complexes with both proteins. This suggested a potential binding interaction between Rg3 and the SIRT1 and NLRP3 proteins.

Effect of SIRT1 inhibitor on HK-2 cell viability and antioxidant capacity. Cell viability was not diminished by the SIRT1 inhibitor Ex527 at concentrations of 10, 20 and 30 μM (Fig. 5C). The co-treatment with CP, Rg3 and Ex527 did not significantly alter cell viability compared with the CP + Rg3 group (Fig. 5D). These results indicated that SIRT1 deficiency did not alter the protective capacity of Rg3 on HK-2 cells.

Compared with the control group, the CP group showed a marked increase in SOD activity, along with a significant decrease in MDA levels and CAT activity (Fig. 5E-G). The combination of CP and Rg3 weakened these effects, with SOD activity being significantly decreased and MDA and CAT

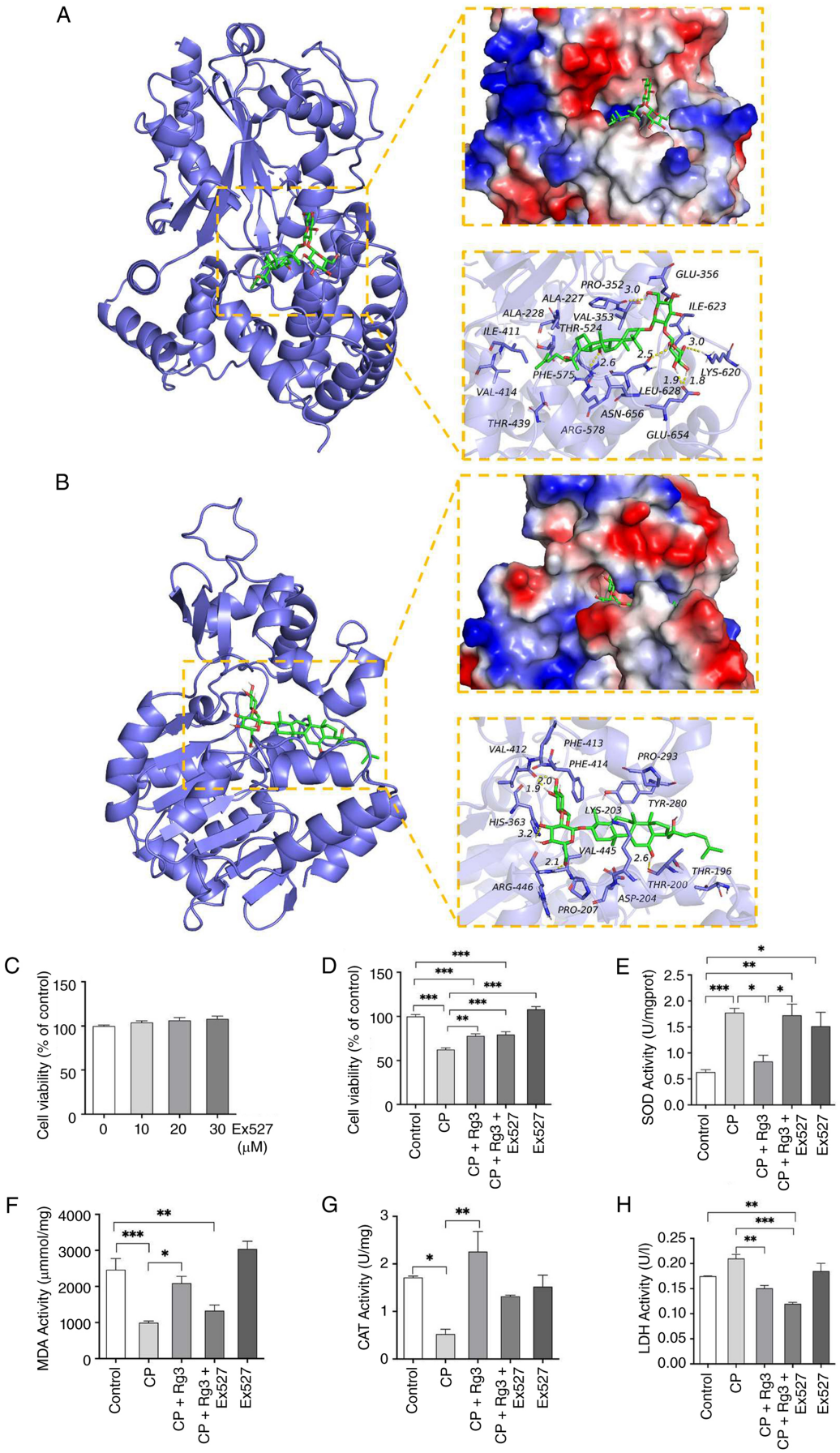

Figure 5. Impact of SIRT1 inhibitor Ex527 on cell viability and antioxidant response of Rg3-treated HK-2 cells. 3D structure of Rg3 and (A) NLRP3 and (B) SIRT1 complexes. (C) Effect of Ex527 (10, 20 and 30 μM) and (D) CP, Rg3 and Ex527 on HK-2 cell viability. Effect of CP, Rg3 and Ex527 on (E) SOD, (F) MDA, (G) CAT and (H) LDH activity. *P<0.05, **P<0.01, ***P<0.001. Sirt, sirtuin; Rg3, ginsenoside Rg3; CP, cisplatin; SOD, superoxide dismutase; MDA, malondialdehyde; CAT, catalase; LDH, lactate dehydrogenase.

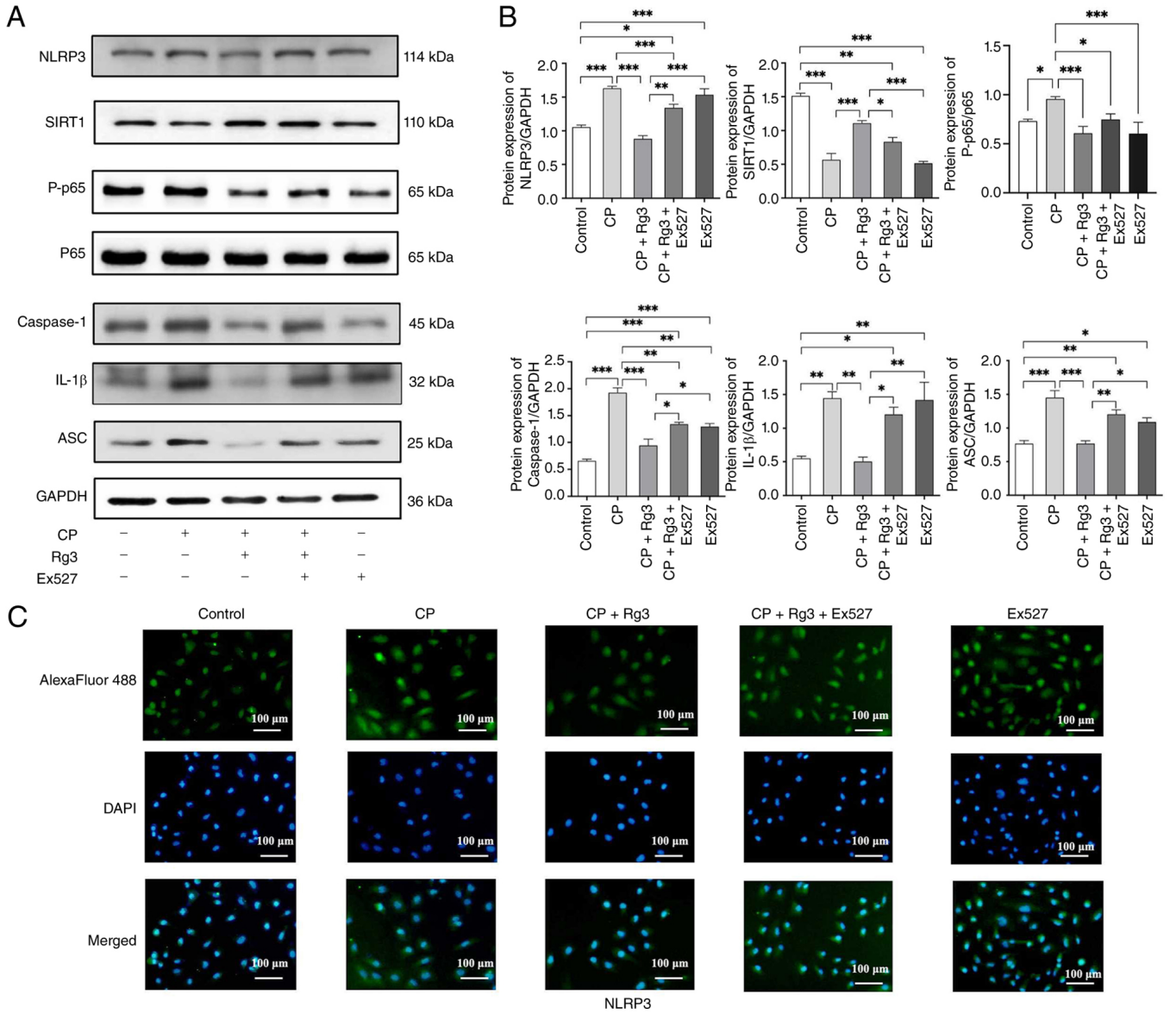

Figure 6. Impact of Ex527 on expression of NLRP3, SIRT1, p-p65, caspase-1, IL-1β and ASC proteins in HK-2 cells. (A) Representative western blot images and (B) Quantitative analysis of western blot data. (C) Immunofluorescence of NLRP3. Magnification, x20. *P<0.05, **P<0.01, ***P<0.001. Sirt, sirtuin; p-, phosphorylated; ASC, apoptosis-associated speck-like protein with CARD; CP, cisplatin; Rg3, ginsenoside Rg3.

activity significantly elevated. However, Ex527 reversed these effects of Rg3.

CP significantly increased LDH release compared to the control group, indicating enhanced cell membrane damage (Fig. 5H). Rg3 co-treatment significantly attenuated CP-induced LDH release, demonstrating its protective effect against CP-induced HK-2 cell injury. However, Ex527 did not reverse the protective effect of Rg3. This results were consistent with the results from MTT assay (Fig. 5D). These findings suggested that SIRT1 deficiency may influence the antioxidant capacity of Rg3 but did not affect its ability to protect against cell damage.

Rg3 and Ex527 modulate CP-induced HK-2 cell injury via the NLRP3 inflammasome. Western blot analysis revealed significant upregulation of NLRP3, p-p65, caspase-1 and ASC protein expression in the CP group compared with the control (Fig. 6A and B). Rg3 mitigated the CP-induced increase in these proteins, suggesting an anti-inflammatory effect. However, Ex527 counteracted the suppressive effects of Rg3, indicating a complex interaction between these compounds. Immunofluorescence (Fig. 6C) demonstrated the impact on NLRP3 expression in HK-2 cells. Nuclei were stained blue, while NLRP3 protein expression was indicated by green fluorescence. CP led to an increase in NLRP3 expression, which was attenuated by Rg3. Ex527 reversed the Rg3-mediated decrease in NLRP3 expression. Collectively, these findings indicated that Rg3 served an anti-inflammatory role by modulating the inflammatory response induced by CP, potentially via the SIRT1 pathway.

Discussion

The combination of CP and Rg3 showed enhanced therapeutic potential against LLC cell proliferation and tumor growth, both *in vitro* and *in vivo*. This combination not only boosts anti-tumor effects but also affects multiple biological

pathways, including the PI3K/Akt/mTOR signaling pathway, NF-κB-mediated epithelial-mesenchymal transition and stemness, immune checkpoint PD-L1 expression, and SOX2-mediated transcriptional regulation, which is important for overcoming drug resistance and enhancing cancer therapy efficacy (13,23-25). The decreased LLC cell viability and migration and tumor size and volume in the CP + Rg3 group suggested inhibition of cell survival. The increased apoptosis, demonstrated by TUNEL assay and histopathological analysis, proves Rg3 ability to augment CP-induced tumor suppression.

Rg3 modulation of apoptotic proteins in the presence of CP points to a potential therapeutic strategy to boost programmed cell death in cancer. VCAM-1 and ICAM-1 are cell surface adhesion molecules expressed on vascular endothelium that mediate leukocyte attachment and migration into tissue during inflammation (26), while MIF is a pro-inflammatory cytokine that activates macrophages and sustains immune responses (27). Collectively, these biomarkers reflect vascular inflammation and endothelial activation. Downregulation of adhesion molecules and inflammatory pathways suggests Rg3 could alter the tumor immune microenvironment, which is key for tumor progression and immune evasion.

In line with our previous study demonstrating that the combination of Rg3 with CP induces protective effects via the modulation of apoptotic and autophagic pathways in HK-2 cells (17), the present study identified two additional, potentially associated contributors: Regulation of OCT2 and P-gp transporters in controlling intracellular CP accumulation and the modulation of the SIRT1-NLRP3 axis in tumor cells. While our previous study (17) established apoptosis and autophagy as key cytoprotective mechanisms under combination therapy, the present findings suggest that regulation of intracellular drug concentration by membrane transporters and SIRT1-dependent inflammatory regulation may serve as complementary or parallel pathways (28,29). The association between SIRT1 and NLRP3 activation represents a potential contributing mechanism rather than a definitively established causal association; further experimental validation, including genetic or pharmacological studies, is required to substantiate its functional role in mediating the therapeutic effects of this combination regimen.

Although Rg3 exhibited favorable docking scores with both SIRT1 and NLRP3, molecular docking only predicts putative binding conformations *in silico* and does not constitute evidence of direct physical interactions in cellular contexts. Future studies should perform co-immunoprecipitation and proximity ligation assays to validate direct SIRT1-Rg3 binding. Although wound healing assay demonstrated cell migration, the present study did not perform Transwell assays to evaluate cell migration capacity. Furthermore, the present study did not perform Annexin V/PI flow cytometry analysis, necessitating the use of cleaved caspase as an alternative apoptosis marker.

The use of the SIRT1 inhibitor Ex527 reveals a complex interplay between Rg3 and SIRT1 in modulating the antioxidant response to CP-induced oxidative stress (22,23). Ex527 partially reversed antioxidant effects without fully abrogating cytoprotection. While Ex527 did not negate Rg3-induced protective effects on cell viability, it did reverse the antioxidant effects of Rg3. Furthermore, Rg3 ability to mitigate the CP-induced upregulation of NLRP3 inflammasome components suggests an anti-inflammatory effect, which was partially reversed by Ex527. SIRT1 may partially contribute to the antioxidant effects of Rg3, but SIRT1-independent pathways may serve key roles. The reversal of Rg3-mediated effects by Ex527 highlighted the regulatory mechanisms and the importance of understanding the interplay between these compounds in the context of inflammation.

While the present study identified SIRT1 modulation as a component of Rg3-mediated NLRP3 suppression in the LLC tumor microenvironment, this may be a potential contributing mechanism rather than a novel pathway. SIRT1 may contribute to the attenuation of NLRP3 inflammasome activation following Rg3 + CP treatment, potentially via context-dependent deacetylation events or metabolic reprogramming within tumor cells. However, the SIRT1-NLRP3 regulatory axis has been previously implicated in diverse inflammatory and oncological settings (30,31). Validation requires targeted interventions such as SIRT1-specific knockdown or pharmacological inhibition *in vivo*. Furthermore, whether this interaction represents a direct molecular target of Rg3 or an indirect consequence of altered cell stress responses warrants detailed mechanistic investigation. Future studies should determine if this pathway functions distinctly in tumor vs. normal kidney tissue, which is key for optimizing the dual benefits of anti-cancer efficacy and nephroprotection, ensuring effective tumor suppression without compromising renal function (17).

Subsequent research should focus on the clinical application of these findings, investigating the potential of Rg3 as a complement to CP chemotherapy to enhance therapeutic efficacy. This includes studying how Rg3 interacts with the SIRT1-NLRP3 pathway and its implications for renal protection and drug resistance modulation.

In conclusion, the present study provided a scientific basis for potential use of Rg3 in mitigating CP-induced nephrotoxicity and enhancing the effects of CP in cancer treatment. Rg3 may serve as a renal protector, anti-inflammatory agent and potentially an anti-tumor therapeutic agent. The present study provided a basis for further exploration and underscores the necessity of elucidating the underlying molecular mechanisms and sustained impact of this combinatorial therapy.

Acknowledgements

The authors would like to thank Dr Xiuzhu Gao, Core Facility of the First Hospital of Jilin University (Changchun, China) for experimental technical support.

Funding

This study was supported by Department of Science and Technology of Jilin Province (grant no. YDZJ202501ZYTS138), Education Department of Jilin Province, China (grant no. JJKH20250215KJ) and Special health personnel of Jilin Province (grant nos. JLSRCZX2025-138 and JLSRCZX2025-025).

Availability of data and materials

The data generated in the present study may be requested from the corresponding author.

Authors' contributions

JZ, LF and SZ conceived and designed the study and wrote the manuscript. YZ and JG performed experiments. JZ and SZ confirm the authenticity of all the raw data. All authors have read and approved the final manuscript.

Ethics approval and consent to participate

All animal care and experimental procedures were approved by the Center for Experimental Animal Research, Institute of Basic Medical Sciences, Jilin University (Changchun, China; approval no. 2023226).

Patient consent for publication

Not applicable.

Competing interests

The authors declare that they have no competing interests.

References

1. Hendriks LEL, Remon J, Faivre-Finn C, Garassino MC, Heymach JV, Kerr KM, Tan DSW, Veronesi G and Reck M: Non-small-cell lung cancer. Nat Rev Dis Primers 10: 71, 2024.
2. Meyer ML, Fitzgerald BG, Paz-Ares L, Cappuzzo F, Jänne PA, Peters S and Hirsch FR: New promises and challenges in the treatment of advanced non-small-cell lung cancer. Lancet 404: 803-822, 2024.
3. Galluzzi L, Senovilla L, Vitale I, Michels J, Martins I, Kepp O, Castedo M and Kroemer G: Molecular mechanisms of cisplatin resistance. Oncogene 31: 1869-1883, 2012.
4. Tang C, Livingston MJ, Safirstein R and Dong Z: Cisplatin nephrotoxicity: New insights and therapeutic implications. Nat Rev Nephrol 19: 53-72, 2023.
5. Gao H, Song Y, Ma J, Zhai J, Zhang Y and Qu X: Untargeted metabolomics analysis of omeprazole-enhanced chemosensitivity to cisplatin in mice with non-small cell lung cancer. Chem Biol Interact 360: 109933, 2022.
6. Kim C and Kim B: Anti-cancer natural products and their bioactive compounds inducing ER stress-mediated apoptosis: A review. Nutrients 10: 1021, 2018.
7. Luo H, Vong CT, Chen H, Gao Y, Lyu P, Qiu L, Zhao M, Liu Q, Cheng Z, Zou J, *et al*: Naturally occurring anti-cancer compounds: Shining from Chinese herbal medicine. Chin Med 14: 48, 2019.
8. Pan L, Zhang T, Sun H and Liu G: Ginsenoside Rg3 (Shenyi Capsule) combined with chemotherapy for digestive system cancer in China: A Meta-analysis and systematic review. Evid Based Complement Alternat Med 2019: 2417418, 2019.
9. Sun M, Ye Y, Xiao L, Duan X, Zhang Y and Zhang H: Anticancer effects of ginsenoside Rg3 (review). Int J Mol Med 39: 507-518, 2017.
10. Peng Z, Wu WW and Yi P: The efficacy of ginsenoside Rg3 combined with First-line chemotherapy in the treatment of advanced Non-small cell lung cancer in China: A systematic review and Meta-analysis of randomized clinical trials. Front Pharmacol 11: 630825, 2020.
11. Wang L, Zhang Y, Song Z, Liu Q, Fan D and Song X: Ginsenosides: A potential natural medicine to protect the lungs from lung cancer and inflammatory lung disease. Food Funct 14: 9137-9166, 2023.
12. Lu Z, Fu Y, Fu Q, Chang Y, Zhang M and Jin T: Ginsenoside RG3 synergizes with STING agonist to reverse cisplatin resistance in gastric cancer. Food Sci Nutr 13: e4744, 2025.
13. Jiang Z, Yang Y, Yang Y, Zhang Y, Yue Z, Pan Z and Ren X: Ginsenoside Rg3 attenuates cisplatin resistance in lung cancer by downregulating PD-L1 and resuming immune. Biomed Pharmacother 96: 378-383, 2017.
14. Wang L, Li X, Song YM, Wang B, Zhang FR, Yang R, Wang HQ and Zhang GJ: Ginsenoside Rg3 sensitizes human non-small cell lung cancer cells to γ-radiation by targeting the nuclear factor-κB pathway. Mol Med Rep 12: 609-614, 2015.
15. Percie Du Sert N, Hurst V, Ahluwalia A, Alam S, Avey MT, Baker M, Browne WJ, Clark A, Cuthill IC, Dirnagl U, *et al*: The ARRIVE guidelines 2.0: Updated guidelines for reporting animal research. J Cereb Blood Flow Metab 40: 1769-1777, 2020.
16. Chen Y, Mao K, Han D, Ma R, Sun T, Zhang H and Han B: Nanomedicine based on chemotherapy-induced immunogenic death combined with immunotherapy to enhance antitumor immunity. Front Pharmacol 15: 1511423, 2024.
17. Zhai J, Gao H, Wang S, Zhang S, Qu X, Zhang Y, Tao L, Sun J, Song Y and Fu L: Ginsenoside Rg3 attenuates cisplatin-induced kidney injury through inhibition of apoptosis and autophagy-inhibited NLRP3. J Biochem Mol Toxicol 35: e22896, 2021.
18. Dho SH, Cho M, Woo W, Jeong S and Kim LK: Caspases as master regulators of programmed cell death: Apoptosis, pyroptosis and beyond. Exp Mol Med 57: 1121-1132, 2025.
19. Bieging KT, Mello SS and Attardi LD: Unravelling mechanisms of p53-mediated tumour suppression. Nat Rev Cancer 14: 359-370, 2014.
20. Smart JA, Oleksak JE and Hartsough EJ: Cell adhesion molecules in plasticity and metastasis. Mol Cancer Res 19: 25-37, 2021.
21. Osipyan A, Chen D and Dekker FJ: Epigenetic regulation in macrophage migration inhibitory factor (MIF)-mediated signaling in cancer and inflammation. Drug Discov Today 26: 1728-1734, 2021.
22. Abbasi M, Lavasanifar A and Uludag H: Recent attempts at RNAi-mediated P-glycoprotein downregulation for reversal of multidrug resistance in cancer. Med Res Rev 33: 33-53, 2013.
23. Wang X, He R, Geng L, Yuan J and Fan H: Ginsenoside Rg3 alleviates cisplatin resistance of gastric cancer cells through inhibiting SOX2 and the PI3K/Akt/mTOR signaling axis by Up-regulating miR-429. Front Genet 13: 823182, 2022.
24. Lee YJ, Lee S, Ho JN, Byun SS, Hong SK, Lee SE and Lee E: Synergistic antitumor effect of ginsenoside Rg3 and cisplatin in cisplatin-resistant bladder tumor cell line. Oncol Rep 32: 1803-1808, 2014.
25. Wang J, Tian L, Khan MN, Zhang L, Chen Q, Zhao Y, Yan Q, Fu L and Liu J: Ginsenoside Rg3 sensitizes hypoxic lung cancer cells to cisplatin via blocking of NF-κB mediated epithelial-mesenchymal transition and stemness. Cancer Lett 415: 73-85, 2018.
26. Gülbahar BN, Aksakal A, Kerget B, Öztürk N, Araz Ö, Uçar EY and Sağlam L: Evaluation of ICAM and VCAM as biomarkers in serum and bronchoscopic lavage samples of lung cancer patients. Clin Transl Oncol: Jan 20, 2026 (Epub ahead of print). doi: 10.1007/s12094-025-04199-z.
27. Spiller L, Zhang L, Gerra S, Stoppe C, Scheiermann P, Calandra T, Lolis E, Panstruga R, Bernhagen J and Hoffmann A: In vivo synergistic enhancement of MIF-mediated inflammation in acute lung injury by the plant ortholog Arabidopsis MDL1. FASEB J 39: e70489, 2025.
28. Wei L, Zhang W, Li Y and Zhai J: The SIRT1-HMGB1 axis: Therapeutic potential to ameliorate inflammatory responses and tumor occurrence. Front Cell Dev Biol 10: 986511, 2022.
29. Zhai J, Tao L, Zhang S, Gao H, Zhang Y, Sun J, Song Y and Qu X: Calycosin ameliorates doxorubicin-induced cardiotoxicity by suppressing oxidative stress and inflammation via the sirtuin 1-NOD-like receptor protein 3 pathway. Phytother Res 34: 649-659, 2020.
30. Arioz BI, Tastan B, Tarakcioglu E, Tufekci KU, Olcum M, Ersoy N, Bagriyanik A, Genc K and Genc S: Melatonin attenuates LPS-induced acute Depressive-like behaviors and microglial NLRP3 inflammasome activation through the SIRT1/Nrf2 pathway. Front Immunol 10: 1511, 2019.
31. Chen Z, He M, Chen J, Li C and Zhang Q: Long non-coding RNA SNHG7 inhibits NLRP3-dependent pyroptosis by targeting the miR-34a/SIRT1 axis in liver cancer. Oncol Lett 20: 893-901, 2020.